Available online www.ejaet.com

European Journal of Advances in Engineering and Technology, 2018, 5(8): 543-558

Research Article ISSN: 2394 - 658X

Thermal analysis of diamond-like carbon coatings synthesized on aluminium 6061 T-91 substrates by laser sintering of nano-diamond powders

Rajeev Nair

Department of Mechanical Engineering, Wichita State University, Wichita, USA - 67260
rajeev.nair@wichita.edu

ABSTRACT

Laser sintering of electrostatic-spray coated nano-diamond powder (size 2-8 nm, nominal thickness 25 µm) on aluminium 6061 T-91 substrate was carried out using a continuous wave CO_2 laser. The optimum laser parameters were experimentally determined to be 200 W (laser power) and 254 mm/s (scanning speed) based on the criterion of maximum hardness of coating. The optimal coating consisted of a mixture of mostly diamond-like carbon (DLC, accounting for a hardness of 2250 kg/mm^2) and some nanocrystalline diamond (hardness of 9000 kg/mm^2). The evidence of DLC formation and its purity was obtained by characterizing the samples with Raman spectroscopy, X-ray diffraction and scanning electron microscopy/energy dispersive spectroscopy. Finite element model (FEM) solutions of one-dimensional thermal energy transport through the powder bed were obtained for these optimal laser parameters. The heat transfer and parametric design capabilities of the FEM code ANSYS® were employed for this purpose. Thermal properties of the diamond powder bed were evaluated and applied in these models. The steady state and transient temperature profiles along the depth of the coating and substrate as well as the time-dependent cooling in the case of transient model were obtained; these model data are used to validate the experimentally-obtained coating thickness and phase transition. Inclusion of convection effects in the models showed negligible changes in the temperature distributions during heating. A hypothesis of the events that occur during laser sintering is postulated based on the evidence obtained from both model and experiment.

Key words: laser sintering, nano-diamond, steady state, transient

INTRODUCTION

Laser sintering (LS) is a manufacturing technique which uses raster scanning of a laser beam to a specific shape, dictated by a computer-aided design solid model, to sinter powder material and thereby produce three-dimensional objects and coatings [1-5]. Sintering normally refers to furnace processes where the powder compacts are heated to elevated temperatures, usually close to its melting point, where diffusion mass transport is appreciable so that binding occurs at the interfacial grain contacts [6]. However, LS process is advantageous over furnace sintering by suppressing the grain growth and particle agglomeration, minimizing the contamination, and reducing the sintering temperature. LS process generates homogeneous and dense layers while furnace sintering produces layers consisting of agglomerates and inter-agglomerate pores. For example, Macedo and Hernandes [7] reported that laser sintering of ceramics produced finer grain size (50% smaller) and much denser (95%) parts than those obtained in electric furnace sintering. In addition, LS process is a line-of-sight technique providing simplicity, flexibility and environmental safety in processing complex shapes while achieving the functionality, dimensional accuracy, smooth surface, and fine microstructure of the components.

In laser sintering, the use of nano-sized particles is quite attractive over micro-sized particles because sintering can be done at substantially lower temperatures. In addition, nanoparticles can absorb laser light much better. Both these effects are partly attributed to large surface area-to-volume ratio of nanoparticles. Furthermore, the melting temperature decreases markedly with particle size reduction in the nanoscale range [8]. Molecular dynamics simulations [9] showed that sintering of nanoparticles proceeds extremely fast due to mechanisms such as dislocation motion, particle rotation and viscous flow in addition to surface and volume diffusion. Consequently, laser sintering would be preferred to match the speed at which nanopowder sintering takes place. Studies of laser sintering of nanopowders indicate the onset of sintering temperature is 0.2-0.3 T_m as compared to 0.5-0.8 T_m for microscale powders where T_m is the melting temperature [9]. Furnace sintering studies of WC/Co showed that nanopowder starts to shrink at much lower temperatures than micropowder and concluded that nanopowder densifies mostly in the solid state while the micropowder densifies in the liquid state [10]. The melting point of diamond is 3800 K. For nanocrystalline diamond powders, temperatures around 800-1200 K (0.2-0.3 T_m) are expected to cause binding along the particle surfaces. However, at these temperatures, nanocrystalline diamond can potentially undergo phase transition to fully graphitic phase if it is held for a longer time such as in furnace annealing, even under an inert gas environment [11].

In this work, laser sintering of ultra-nanocrystalline diamond powders (2-8 nm) on aluminium 6061 substrate was performed to create a fairly thick layer of diamond-like carbon (DLC), alternatively known as tetrahedral-amorphous carbon films. DLC exhibits high hardness due to the significant fraction of sp^3 hybridized carbon atoms [12]. DLC has many potential applications due to their superior thermal, electronic, optical, mechanical and tribological properties [13-16]. In this paper, experimental results of DLC coating formation, coating thickness, size of heat affected zone and adhesion strength are corroborated with finite element solution of thermal energy transport models which take into account laser energy absorption, powder densification, heat conduction and convection. We have utilized one-dimensional (1-D) steady and transient heat flow models to explain the observed results. It may be noted that there are several complex and elegant analytical and numerical models (1-D to 3-D) available for predicting the effects of laser-induced heating. However, one-dimensional models can adequately describe the events that take place in laser material processing. For example, Dabby and Paek presented a transient one-dimensional model considering the penetration of radiation into the material [17]. Noguchi, *et al.* applied the enthalpy method to formulate a one-dimensional volumetric heating model and solved it using a finite element technique [18]. Mazhukin, *et al.*analysed the volume overheating of solid and liquid phases in pulsed laser evaporation of superconducting ceramics using a one-dimensional model [19].

METHODS & MODELING

Sample coupons of aluminium alloy 6061-T91 with a size of 25 mm x 25 mm x 9.5 mm were prepared by cutting and grinding from a large plate stock. Nano-diamond powders produced by shock detonation synthesis, with a size range of 2-8 nm and purity of 90% or better were electrostatically sprayed on the aluminium coupons and the deposition process was carefully controlled so as to get a uniform and homogenous coating with a nominal thickness of 25 µm. A high-power continuous wave CO_2 laser (*820 Spectra – Spectra Physics®*) was then used to densify and sinter the diamond powders (Figure 1). A focused rectangular beam (length of 1 mm by width of 0.1 mm) obtained by a cylindrical lens was chosen for the process. The laser beam in raster scan configuration, controlled by a programmed CNC controller, was used to sinter the nanoparticles. Argon was used as the assist gas during the sintering process. Numerous laser parameter variations such as laser power and scan rate were attempted. The optimum laser parameters were determined based upon the criterion of maximum hardness and listed in Table 1.

Table -1 Optimal Process Parameters

Parameter	**Value**
Laser power, Watt	200
Focal length of lens, mm	127
Beam size at the powder surface, mm^2	1 x 0.1
Scanning speed, mm/sec	254
Standoff distance from the nozzle to the substrate, mm	15
Overlap among passes, %	15-25
Assist gas flow rate, $m^3/s(*10^{-4})$	3.15

Following laser sintering, the coatings were evaluated for densification, phase transformation, hardness, coating thickness and coating/substrate interface strength. Detailed examination of the coating using a variety of instruments [presented in R. Nair et al.] revealed >99% dense mixture of DLC (>90%) and diamond phases for a nominal thickness of 10 µm, and average hardness of 2250 kg/mm^2.A few regions exhibited hardness of nearly 9000 kg/mm^2. Figure 2 shows a scanning electron micrograph showing the regions of coating, heat affected zone (HAZ) and substrate. The term "depth" used in the later sections of the paper imply the thickness of the coating and the melt depth of aluminiumsubstrate. HAZ is essentially a zone of overaging in precipitation hardened alloys where the precipitates become coarse and the material becomes quite heterogeneous. Consequently, the etchant aqua regia had a severe attack through ensuing chemical reactions and creating etch pits.

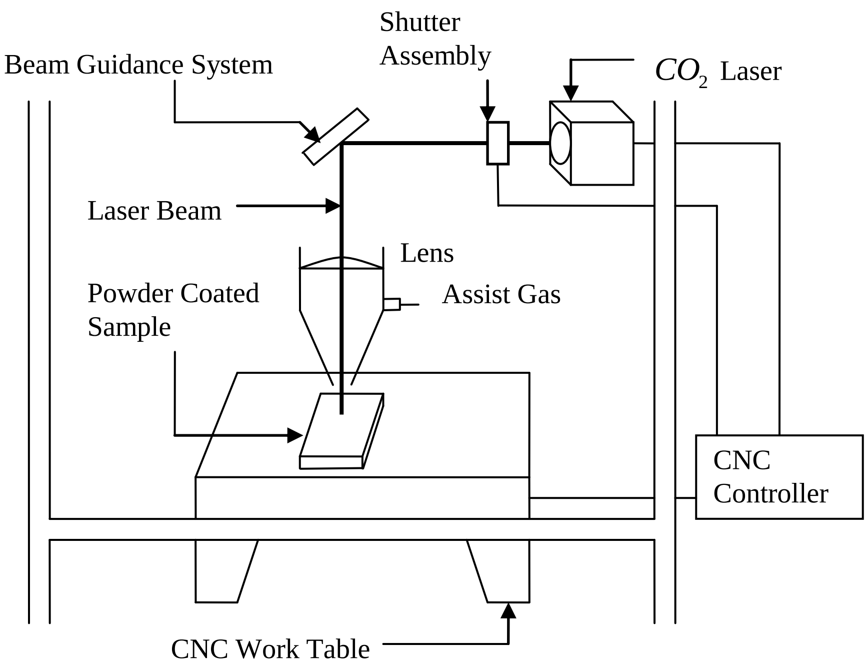

Fig. 1 Schematic diagram of the direct laser-sintering process

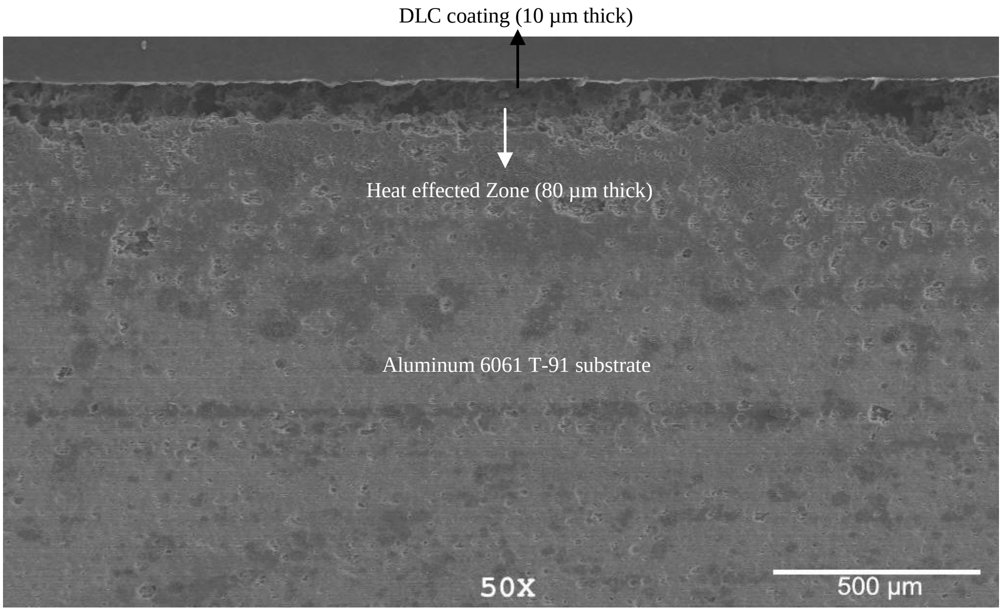

Fig. 2 SEM micrograph of the transverse section of the coating

Thermal energy transport model description

Laser sintering involves several physical phenomena including energy absorption, heating of the powder, binder melting, densification and sintering of particles. Laser power, energy distribution, spot size, beam speed, and extent of overlapping control these phenomena. The incident angle of the beam is kept normal to the powder bed source to minimize the reflective energy losses. Multiple scattering occurs and helps in a nearly homogeneous distribution of the radiation in the powder bed. Energy absorption is also enhanced by the powder porosity. Densification begins in the solid state based on the hypothesis that the nanoparticles rearrange rapidly and diffusion rate is much higher. In contrast, the sintering behaviour of micropowders is such that there is no measurable shrinkage until close to the melting point where densification becomes rapid and the specimen is fully sintered by liquid-phase [10]. It is also possible that the laser energy heats and melts the aluminium substrate and enough liquid is produced to achieve liquid-phase sintering with an inter-particle connection to minimize surface energy. In thermal analysis, the individual diamond particle is considered as a dense material while the surrounding air is approximated by a low thermal diffusivity continuum. The process model has several parts as described below.

Properties of Powder Bed, Substrate and Assist Gas

Powder Bed: The ultra-nanocrystalline diamond powder had <10% metallic and graphitic impurities and moisture. Electrostatic spray resulted in an average thickness of the powder bed as 25 µm. The degree of packing of a powder bed is characterized by the relative density, ρ_R defined as:

$$\rho_R = \frac{\rho}{\rho_s} \tag{1}$$

, where ρ is the density of the powder bed and ρ_s is the theoretical density of the solid. The determination of actual powder bed density is an uncertain process. There are some idealized extremes, one of which involves the assumption that all the solid particles in the powder are spheres of equal size/density arranged in a cubic array. In such a case the bed density is given by $\rho = \frac{\pi\rho_s}{6}$, and hence ρ_R becomes 52.3 % [21]. The porosity content can be estimated from the porosity parameter as:

$$\varphi = 1 - \rho_R = 0.477 \text{ or } 47.7\%. \tag{2}$$

Actual powder beds in laser sintering exhibit porosities between 40 and 60% [21]. It is assumed in our study that the porosity is 55%, which makes the porosity parameter $\varphi = 1 - \rho_R$ =0.55. Since the solid theoretical density of polycrystalline diamond is $\rho_s = 3500\frac{kg}{m^3}$ and ρ_R =0.45, the density of powder bed becomes $\rho = 1575\frac{kg}{m^3}$. When the powder particles are composed of the same material and voids are filled with air, the specific heat capacity C_p of the powder bed is practically same as the solid particles [22-24], which in this case, is composed of ultra-nanocrystalline diamond powders.

Heat transfer through powder bed mainly occurs through conduction and radiation since inter-particle distances are too small to permit convection heat transfer. Powder particles are separated by gas in the bed and since gases have smaller thermal conductivities at room temperature, the thermal conductivity of a powder bed is essentially dictated by the gas (air in this case) embedded within the voids [23, 25]. Effective thermal conductivity of a powder bed including radiation, convection and conduction effects was given by Yagi and Kunii [26] as,

$$K_{eff} = \frac{\rho_R K_s}{\left(1 + \frac{\phi K_s}{K_g}\right)} \tag{3}$$

Where, K_s is the solid thermal conductivity, K_g is the thermal conductivity of air which surrounds the diamond nanoparticles and ϕ is an empirical coefficient given by:

$$\phi = 0.02 * 10^{2(0.7-\rho_R)} \tag{4}$$

Temperature-dependent numerical values of specific heat and effective thermal conductivity of the powder bed used for the finite element modelling are enumerated in Table 2. These properties are assumed to be constant after 1100 K unless phase change occurs.

Substrate: Aluminium 6061 T-91 was selected as the substrate in this study for a number of reasons. It is an excellent structural material with beneficial characteristics such as light weight, good strength and high corrosion resistance. It is also a good substrate material for deposition of coatings. It is used in a wide variety of products and applications [30, 31]. Properties of aluminium 6061 T-91 used in thermal analysis are listed in Table 3. However, it lacks tribological properties for which DLC coatings would be most desired [32].

Assist Gas: Argon, used as the shield gas during laser sintering, creates convection heat transfer. Hence, it is imperative to calculate heat transfer coefficient (*h*) of argon. In order to calculate *h*, the surface temperature must be known. For this purpose we have assumed a surface temperature of 1200 K (based on transient heat conduction model that will be shown later). The film temperature, T_f is the average of the surface temperature and the ambient temperature (300 K).

Table -2 Some thermo-physical properties of the powder bed [27-29]

Temp. (K)	K_s (W/m K)	K_g (W/m K)	K_{eff} (W/m K)	C_p (J/Kg K)
300	2050	0.0262	0.1864	500
400	1500	0.0338	0.2404	875
500	1250	0.0407	0.2894	1125
600	1000	0.0469	0.3335	1375
700	950	0.0524	0.3725	1525
800	900	0.0575	0.4087	1700
900	850	0.0626	0.4449	1750
1000	850	0.0676	0.4804	1800
1100	850	0.0726	0.5159	1850

Table -3 Thermo-physical properties of aluminum 6061 T-91 [30]

Temp. (K)	K (W/m K)	C_p (J/Kg K)
300	170	892
400	175	947
500	170	993
600	165	1047
700	160	1086
800	155	1148
900	150	1226

$$T_f = \frac{T_S + T_A}{2} = 750K \tag{5}$$

Dynamic viscosity and density of argon at 750 K are 44.5*10^{-6} kg/ms and 1.784 kg/m^3 respectively [25]. Hence the kinematic viscosity is,

$$\nu = \frac{\mu}{\rho} = 24.94*10^{-6}\,\frac{m^2}{s} \tag{6}$$

It is necessary to find whether the flow of argon gas over the diamond powder is a laminar or turbulent one. Hence the Reynolds number is calculated as follows.

$$\mathrm{Re}_L = \frac{u_\alpha L}{\nu} \tag{7}$$

, where u_α is the flow velocity of argon gas and L is the plate length over which the gas flows. u_α is 27.59 m/s for a gas flow rate of 3.15*10^{-4} m^3/s through a pipe of diameter 0.00381 m and L is 0.0254 m. This gives a Reynolds number of 28,100 which is well below 100,000 necessary for developing full turbulent flow over a flat plate [25].

For a flat plate in parallel flow [25],

$$\overline{Nu_L} = 0.664\,\mathrm{Re}_L^{0.5}\,\mathrm{Pr}^{0.33}, \mathrm{Pr} \geq 0.6 \tag{8}$$

$$\mathrm{Pr} = \frac{\nu}{\alpha} = \frac{\mu C_p}{K} \tag{9}$$

C_p and K for argon at 750 K are 520.5 J/kg K and 0.0353 W/m K respectively, giving a Prandtl number of 0.6561 and hence the Nusselt number becomes 93.8.

The heat transfer coefficient, *h*, is now calculated from $h = \frac{Nu_L K}{L}$ as 130.35 $\frac{W}{m^2 K}$

Energy Input Sub-model

Duration of laser irradiation τ for a line beam of L_b x W_b is,

$$\tau = \frac{L_b}{V_s} \tag{10}$$

, where L_b is the length of focused beam, W_b the width and V_s is the beam speed. For L_b = 1 mm, V_s = 254 mm/sec, τ is 0.0039 sec. Next step is to find out the power absorbed by the powder bed surface, P' which is related to the beam power, P, as follows [33].

$$P' = \chi P - \varepsilon\sigma\left(T_S^4 - T_A^4\right) \tag{11}$$

Neglecting radiation losses (second term on the right side of equation 11), and based on gray body approximation wherein emissivity of a body is equal to its absorptivity, we obtain,

$$P' = \varepsilon P \tag{12}$$

Emissivity of the powder bed can be derived from the following equation:

$$\varepsilon = A_H \varepsilon_H + \left(1 - A_H\right)\varepsilon_S \tag{13}$$

, where A_H is the area fraction of the surface that is occupied by the radiation-emitting holes, ε_H is the emissivity of the hole and ε_S is the emissivity of the solid particle (nanocrystalline diamond).

For the CO_2 laser (infrared) emitting a laser beam at a wavelength of 10.6 µm, the reflectance, R of a diamond particle surface is 0.1668 [34]. Assuming that the rest is absorbed, the solid emissivity ε_S becomes 0.8332. A_H is based on the porosity parameter φ and is given as,

$$A_H = \frac{0.908\varphi^2}{1.908\varphi^2 - 2\varphi + 1} \text{ and for a } \varphi \text{ of 0.55, } A_H = 0.5756$$

Emissivity of the hole, ε_H is dependent on ε_S and φ by the following equation,

$$\varepsilon_H = \frac{\varepsilon_S\left[2 + 3.082\left(\frac{1-\varphi}{\varphi}\right)^2\right]}{\varepsilon_S\left[1 + 3.082\left(\frac{1-\varphi}{\varphi}\right)^2\right] + 1} = 0.953$$

$$\varepsilon = A_H \varepsilon_H + \left(1 - A_H\right)\varepsilon_S = 0.9022$$

For incident laser power of 200 W and emissivity of 0.9022, the power absorbed by the powder bed surface, P', is, 180.44 W. Power density (or the heat flux) is given as power over the spot area. For a rectangular beam of length and width 1 mm by 0.1 mm and a laser power of 180.44 W, the heat flux, $\ddot{Q}$ turns out to be $1804.4*10^6 \frac{W}{m^2}$

Heat transfer Sub-model

The first law of thermodynamics states that thermal energy is conserved. For a differential control volume associated with laser beam melting of diamond powder, heat transfer problem can be mathematically described as [25]:

$$\rho_{bed} C_p \frac{\partial T}{\partial t} = \nabla\left(K_{eff} \nabla T\right) + Q_g \tag{14}$$

The term on the left represents energy storage, the first term on the right provides the three-dimensional heat conduction and the second term on the right corresponds to the internal heat generation due to laser irradiation. ρ_{bed} is the temperature-dependent density; C_p the specific heat; *T* the temperature; *t* the time and ∇ represents the divergence operator. The material is assumed to be homogeneous.

The laser energy is distributed as near Gaussian according to the laser manufacturer specification. However due to multiple scattering of powder particles in the bed, it is assumed that the laser power is uniform along the spot size and remains constant throughout the laser-material interaction time. Hence considering a uniformly distributed heat source of laser intensity, quantity of heat generation (W/m^3) can be written as,

$$Q_g = \frac{\ddot{Q}}{s} \tag{15}$$

Figure 3 depicts a three-dimensional representation of the model. In this work, we have considered only a one-dimensional equation as it is deemed adequate for the purpose intended, namely determining both steady state and transient temperature profiles as a function of depth that result from the moving heat source by the raster scan of laser beam.

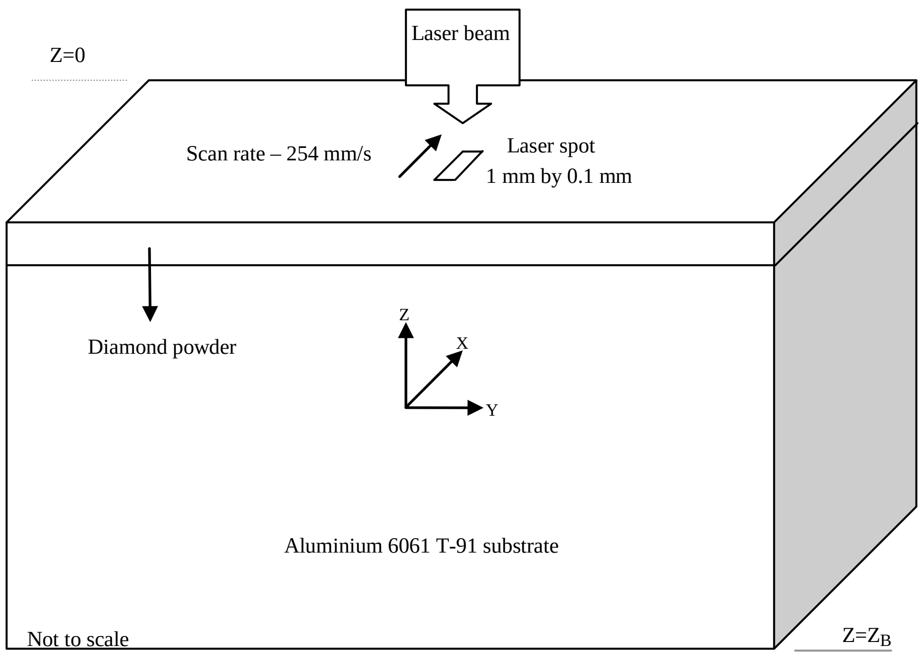

Fig. 3 Three-dimensional representation of the thermal model

One-Dimensional, Steady-State Formulation: In the steady state case the heat conduction equation becomes,

$$\frac{\partial}{\partial z}\left(K_{eff}(T)\frac{\partial T}{\partial z}\right) + Q_g = 0 \tag{16}$$

The boundary conditions are,

$$-K_{eff}\frac{\partial T}{\partial z}\Big|_{z=0} = 0 \text{, neglecting convection \& radiation} \tag{17}$$

$$-K_{eff}\frac{\partial T}{\partial z}|_{z=z_B}=0 \tag{18}$$

One-Dimensional, Transient Formulation: In a one-dimensional transient condition, the heat diffusion equation 14 reduces to,

$$\rho_{bed}(T)C_p(T)\frac{\partial T}{\partial t}=\frac{\partial}{\partial z}\left(K_{eff}(T)\frac{\partial T}{\partial z}\right)+Q_g \tag{19}$$

Following boundary conditions are applied:

Case 1:Convection is considered but radiation is neglected

$$-K_{eff}\frac{\partial T}{\partial z}|_{z=0}=h\left(T_{z=0}-T_{env}\right) \tag{20}$$

, where h is the convection coefficient of argon and T_{env} is the ambient temperature.

Case 2:Both convection and radiation are neglected

$$-K_{eff}\frac{\partial T}{\partial z}|_{z=0}=0 \tag{21}$$

For both cases, no heat is assumed to be lost at the bottom of the aluminium substrate of thickness z_B and hence,

$$-K_{eff}\frac{\partial T}{\partial z}|_{z=z_B}=0 \tag{22}$$

The following initial condition is also applied to recognize the existence of uniform temperature, T_0 , throughout the powder bed prior to the laser sintering process,

$$T(z,0)=T_0 \tag{23}$$

Thermal conductivity K and specific heat C_p are temperature-dependent properties in the powder bed and hence Tables 2 and 3 are used to solve the non-linear heat conduction equation.

Finite Element Solution Procedures

Solving the heat transport equations along with material properties in ANSYS® code yields the time-dependent temperature distribution throughout the powder bed. One-dimensional conduction elements called “link 32” were used for conduction between nodes, and convection element called “link 34” was used for simulating the convective heat transfer between the top of the coating and the argon shield gas. The material properties of nanocrystalline diamond powder and aluminium 6061 T-91 were used. The aluminium alloy substrate of $9.525*10^{-3}$ m long was represented by 10 elements (10 nodes), each element being $9.525*10^{-4}$ m long. The 25 µm thick electrostatic-sprayed, nano-diamond powder on the aluminium alloy substrate was represented by 5 elements, each 5 µm long. There was a common node at the interface. The spot size area of 0.1 mm^2 was incorporated as a real constant. The bottom of the substrate was assumed to be at room temperature of 300 K with no heat loss (fully insulated).

Assumptions

1. The input heat flux due to laser irradiation is treated as an internal heat generation in the powder layer.
2. To simplify the calculation the whole powder layer is considered to be homogenous and continuous.
3. The powder layer is assumed to be subjected to plane stress type of temperature variation as the powder thickness is very small.
4. Effects of radiation are negligible (because low temperatures are required for laser sintering of nano-particles) and hence ignored.
5. Material properties are dependent upon temperature.

6. Laser beam transmission, deflection and scattering losses are ignored.
7. Laser beam energy is assumed uniform over the spot size and normal to the surface.
8. Absorbed laser energy is converted to thermal energy instantaneously.
9. Losses due to ablation of the sample surface, if any, are ignored.
10. Room temperature is assumed to be 300 K.

RESULTS AND DISCUSSION

Characterization

Raman Spectroscopy: A micro-Raman spectroscope (*Ramascope, Reinshaw 1000*) using monochromatic light of wavelength 488 nm was used to characterize the coating. Natural diamond exhibits a sharp first order peak in the Raman spectrum at 1332 cm^{-1}. For the laser-sintered diamond sample (200 W, 254 mm per second), the Raman Shift shows a broad band over the range of 1200 to 1600 cm^{-1}, characteristic of amorphous carbon (Figure 4). Broadening of the diamond band is a result of decreased grain size (nanometer scale) and impurities. A strong, narrow first order diamond peak, located close to 1332 cm^{-1}, and a lack of features attributable to non-diamond forms usually indicates that the material is of good quality. Since nano-diamond powder used in this work has a purity of 90% or better, a strong, narrow first order peak was not visible. In addition, graphitic inclusions can 'screen out' the diamond signal from diamond regions deeper in the sample making the Raman spectrum to indicate a worse quality material than is actually the case.

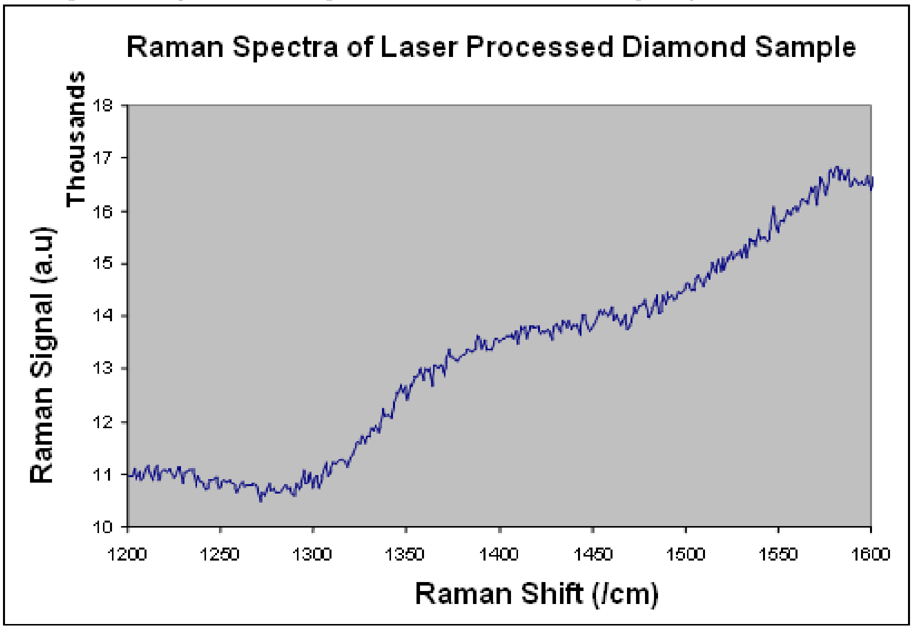

Fig. 4 Raman spectrum of laser-sintered sample

X-ray diffraction (XRD): XRD patterns for the laser-sintered sample proved the existence of DLC coating on the aluminium substrate (Figure 5). The data obtained showed only trace amounts of the DLC phase as expected, because the X-rays penetrate deep into the substrate material as well (since a thin film XRD was not done). XRD diffractrogram clearly shows a DLC peak at Two-Theta (deg.) of 26.61. The remaining peaks represent the reflection of X-rays from the aluminium alloy substrate (face centred cubic (FCC) structure, orientations other than FCC) and the silicon in aluminium 6061.

Scanning Electron Microscopy (SEM) and Energy dispersive spectroscopy (EDS): The coated sample was mounted on Bakelite and then polished and etched (Aqua Regia). A very thin layer of gold was applied (*DENTON® sputter coater*) on the sample for better resolution and signal quality and then examined under an SEM. The coating is seen to be fairly uniform, dense and smooth, free from crack, porosity and inclusions. SEM micrographs of the top surface (Figure 6) of the laser-sintered samples showed some globules as a result of melting and resolidification of impurities. EDS (Energy dispersive spectroscopy) spectrum displayed trace amounts of iron, magnesium and silicon, which were reported to be impurities in the synthetic diamond nanopowder.

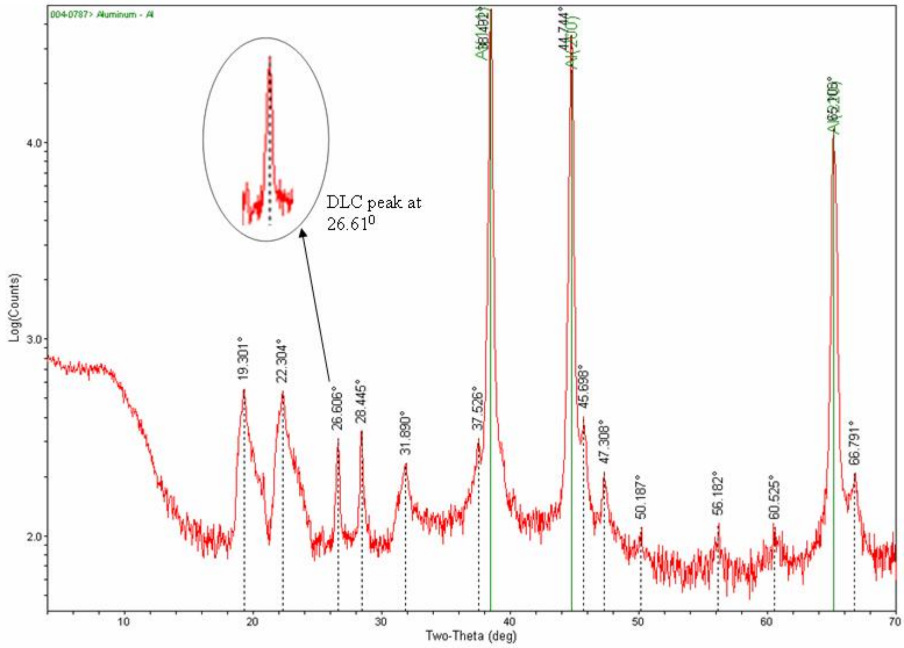

Fig. 5 XRD diffraction pattern of laser-sintered sample using copper K_{α} radiation

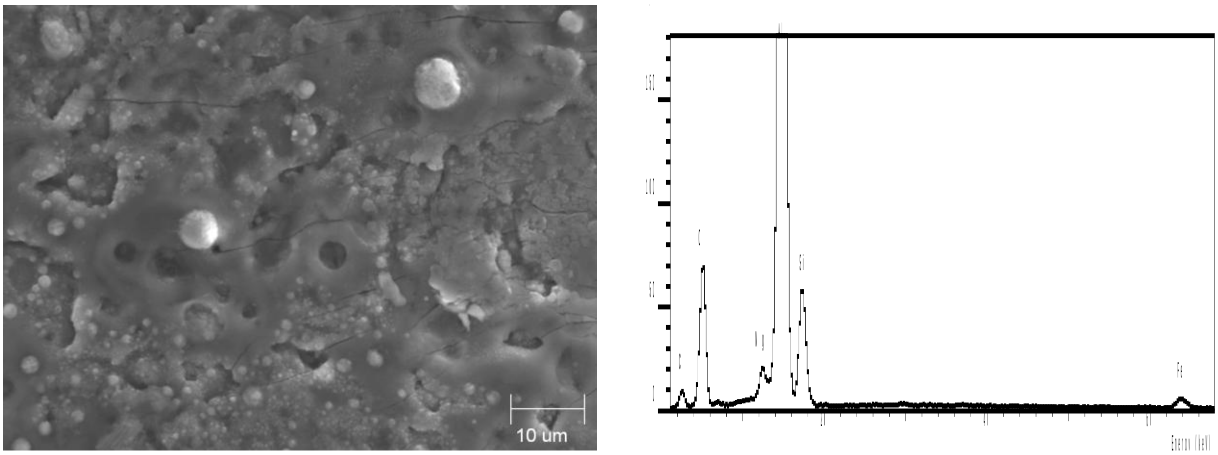

Fig. 6 SEM micrograph of a featureless coating at 7,000X and EDS spectrum

One-dimensional steady state results

Laser sintering is not a steady state process. But to understand the steady state mode of heat transfer in a powder bed, this hypothetical analysis is performed. As is well known, there is no dependence of temperature on time or thermal diffusivity in steady state. The effects of change in density, thermal conductivity and specific heat of the powder bed along with the phase transition to DLC are not accounted for in this model. Despite all these deficiencies, the steady state analysis is capable of providing a quick estimate of temperature distributions, DLC formation and coating depth. Figures 7 and 8 shows the temperature-depth profile obtained in this work.

The temperature at the top surface of the coating is about 2450 K and average temperature of about 1500 K can be seen within the coating depth. The phase transition of diamond to DLC usually occurs in this temperature range for micropowders (lower for nanopowders). For example, studies of the high-temperature transformation of diamond to graphite performed on micro-sized diamond powders revealed that specimens which were heated below 1500 K remained as diamond while those which had been heated to above 1500 K but below 2300 K transformed into a mixture of diamond, DLC and graphite [35, 36].

Diamond is thermodynamically unstable form of carbon. At high temperatures, diamond transforms to other forms of carbon. Based on the traditional phase diagram of carbon, the general expression of the fraction of diamond to transform to graphite, f_g, as a function of temperature and pressure is given by [37]:

$$f_g = \exp\left[-\left(\frac{E_a}{RT}\right)\right] - \exp\left[\frac{-\left(E_a - \Delta G^g_{T,P}\right)}{RT}\right] \quad (24)$$

$$\Delta G^g_{T,P} = 1.77*10^{-6}\left(2.73*10^6 T + 7.23*10^8 - P\right) \quad (25)$$

Where E_a is the activation energy equal to 120 kJ/mole, R is the gas constant 8.31 J/mole K and P is the pressure in Pa. Application of this equation in the present study (P =100,000 Pa, T = 1500 K) yields f_g= 0. However, the particle size dependence is not shown in these expressions. Figure 9 shows the phase diagram of ultra-fine carbon [38] where the particle size is assumed to be 100 nm in the horizontal plane. This diagram illustrates that the diamond is more thermodynamically stable than graphite particularly when the particle sizes are less than 3 nm. Thus, it is inferred that the use of diamond nanopowders can minimize the phase transition to graphite at high-temperatures.

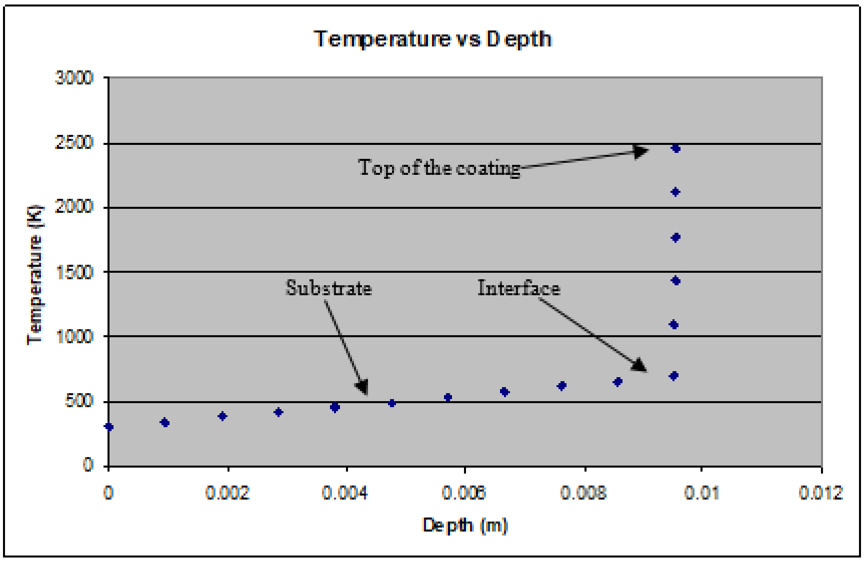

Fig. 7 Temperature profile for one-dimensional steady state analysis (boundary conditions equations 17, 18 and initial condition equation 23)

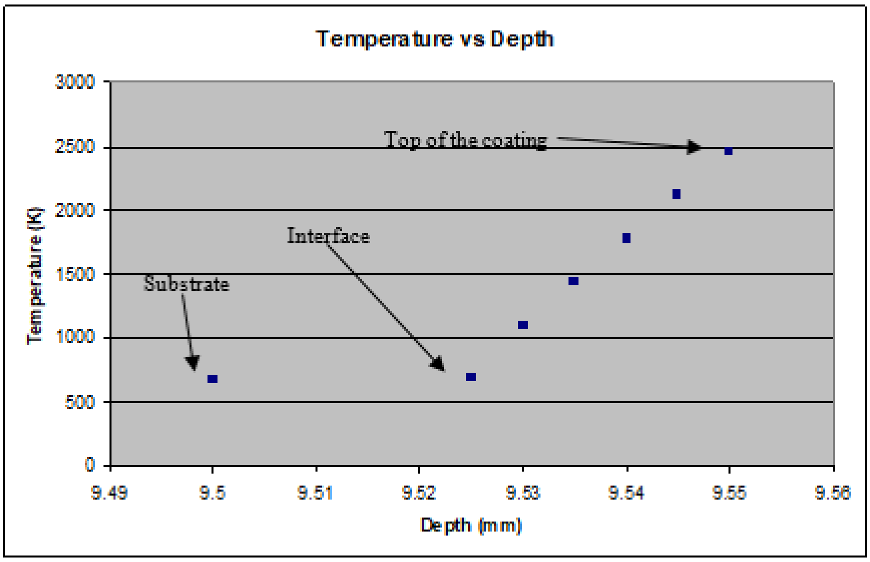

Fig. 8 Temperature profile for the steady state analysis for the coating region (from the top of the coating to just below the interface in figure 4) (boundary conditions equations 17, 18 and initial condition equation 23)

The issue of phase transition from nanocrystalline diamond to DLC warrants explanation. There are three means by which crystalline diamond can be transformed into amorphous carbon: 1) *Melting and rapid quenching of diamond crystals* - Lee *et al.* [39] used molecular dynamics simulations to demonstrate the formation of amorphous structure of carbon by rapid quenching of the melted diamond lattice from 10,000 K at various cooling rates from 1.25×10^{15} K/s to

$6.25x10^{15}$ K/s. This method of phase transition is unlikely in the present work because both temperatures and cooling rates obtained are much lower; 2) *Ion beam irradiation* - Reinke*et al.* [40] studied the effects of ion irradiation on the surface structure of polycrystalline diamond using photoelectron spectroscopy and found that a gradual change from diamond to amorphous carbon occurred for certain ion doses. The tendency of diamond surface to amorphize rather than graphitize under ion irradiation is essentially to do with the type defect structures generated.

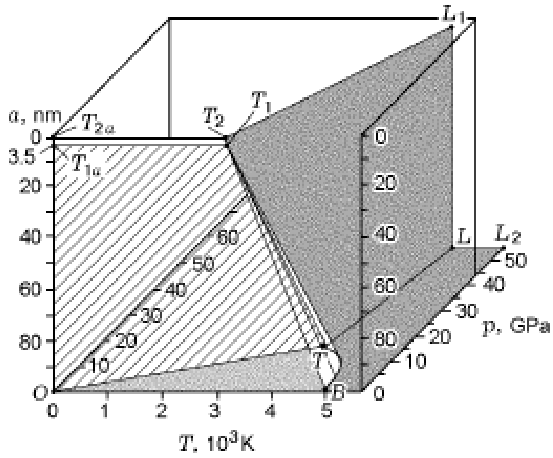

Fig. 9 Phase diagram of ultrafine carbon [37]: $OBTT_1T_{1a}$ is the existence domain of the graphite phase, OTT_1T_{1a} is the interface between the graphite and diamond phases, BTT_1 is the interface between the liquid carbon and graphite phases, and TT_2L_1L is the interface between the liquid carbon and diamond phases

This type of mechanism is again ruled out in our present work because the laser beam does not exert momentum as much as ions; 3) *Annealing* – Nistor*et al.* [41] subjected polycrystalline diamond to furnace annealing in vacuum at temperatures of 1623–1723 K and then examined the changes by optical absorption, Raman spectroscopy, transmission electron microscopy and electron energy loss spectroscopy. The formation of amorphous carbon and/or of well-crystallized graphite layers was observed along grain boundaries. The diamond-to-graphite transition occurred in such a way that three (111) diamond planes transform into two (0002) graphitic sheets. This type of mechanism is probable in our work where the temperatures are quite similar. However, rapid heating and cooling associated with laser sintering caused diamond transformation to DLC rather than graphite. Furthermore, the fact that phase transition takes place at the grain boundaries during annealing implies that nanoparticles would provide large number of sites for the formation of amorphous carbon. Another interesting observation in the temperature plot (Figures 7 and 8) is the interface temperature of 700 K, which is close to the melting point of aluminium 6061 T-91 (855 K). The sintering process is culminated when the aluminium alloy starts melting at 855 K along the interface and diffuses into the lower part of the sintered coating.

One-dimensional transient state results

The temperature profiles along the depth with and without convection are shown in Figures 10 and 11. Convective heat transfer by argon gas has an insignificant effect. The temperature at the top node representing DLC layer is reduced only by 1.23% while it is even less (0.003%) at a node representing the surface just below the substrate-alloy interface. A comparison with steady-state analysis indicates the following: 1) the slope of heating curve in the coating portion is exponential for transient and linear for steady-state; 2) the transient analysis shows that the top surface exhibits a temperature of 1275 K and 1258 K without and with convection respectively as opposed to 2450 K in the steady state; 3) the transient analysis also predicts much lower temperatures at the coating-substrate interface. This substantial reduction in temperatures compared to the steady state is explained below. Since each section of the powder bed collapses through densification as it reaches its sintering temperature, there is a subsequent reduction in the depth of the coating and an increase in density and thermal conductivity. There is also the formation of DLC phase which could change some of the assumed properties of the diamond nanopowders. In FEM, it is assumed that the powder bed is remaining with the same thickness until the end of laser beam passage. But in reality, the powder bed is compacted from 25 µm to 10 µm during laser processing. This reduction in 16 µm is not accounted for in the FEM solution. In order to correct these deficiencies, an iterative process that assigns different fractions of laser beam interaction time to densification and heating of DLC was employed to refine the transient model. The condition used in this iterative procedure is the experimental observation that the coating-substrate interface has reached the melting temperature of aluminium alloy. Thus the formulation problem is as follow: During the X fraction of the interaction time of the beam with powder bed, adequate temperatures have reached for initiation of nanoparticle sintering and for densification of powders to completion followed by phase transition from diamond powder to DLC.

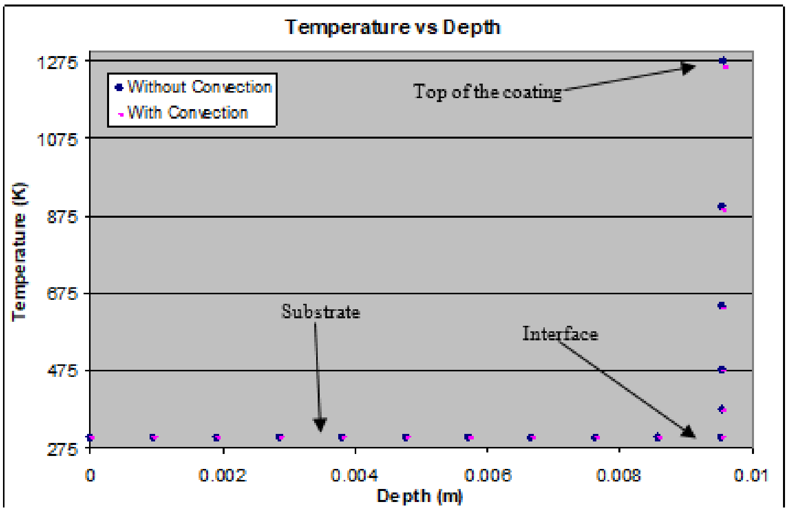

Fig. 10 Temperature profile for transient analysis at t = 0.0039 s (boundary conditions equations 20, 21, 22 and initial condition equation 23)

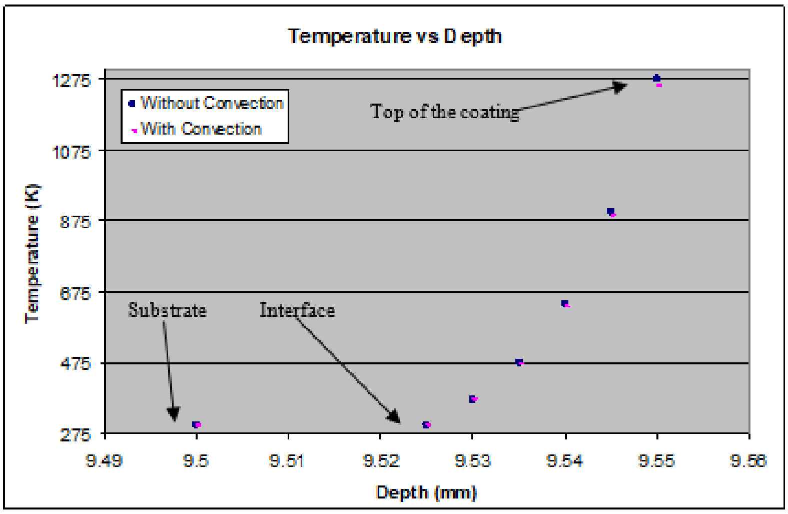

Fig. 11 Temperature profile for transient analysis of the coating region (from the top of the coating to just below the interface in figure 7) at t = 0.0039 s (boundary conditions equations 20, 21, 22 and initial condition equation 23)

The depth of coating is reduced from 25 µm to 10 µm in this stage. Density of the powder bed increases as material flow into voids, causing a decrease in overall volume. Mass transfer occurs during this phase that reduces the total porosity by repacking, followed by material transport due to diffusion. Atoms move along crystal boundaries to the walls of internal pores, redistributing mass from the internal bulk of the object and smoothing pore walls. During the Y fraction of the interaction time of the beam with sintered DLC (note that X+Y=1), heating continues to a point where melting and overaging of aluminium alloy takes place at and below the coating interface. The conversion of diamond nanopowder into amorphous carbon form occurs around 940 K [42] at ambient pressure in fast pace due to large surface area of nanoparticles and non-equilibrium nature of laser sintering. The revised transient analysis (with convection) provided X as 0.75 and Y as 0.25. The temperatures at the top three nodes in the transient model after 75% of the laser interaction time are chosen as the initial conditions. The coating thickness of 10 µm is represented by 2 elements each 5 µm long having thermal properties of tetrahedral amorphous carbon (ta-C) which is one of the forms of DLC [43]. Heat is supplied for the remaining 25% of the laser interaction time and the final temperatures are calculated and shown in Figure 12. The substrate-coating interface temperature obtained is just below melting temperature of the aluminium alloy. At 80 µm below the substrate-coating interface is the heat affected zone (HAZ)-substrate interface where the temperature is close to 430 K. The average temperature in the HAZ is large enough to support the possibility that overaging process can occur in this zone.

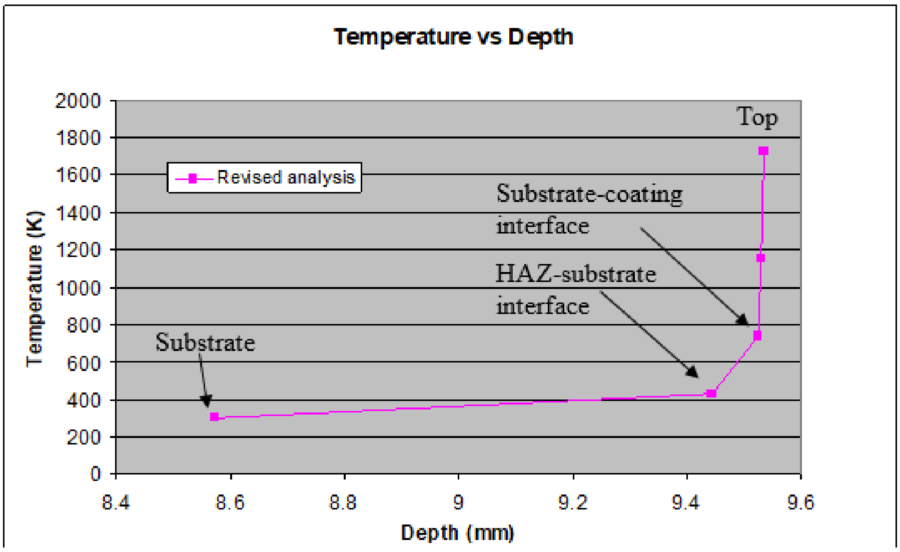

Fig. 12 Revised analysis: Temperature plot at t = 0.0039 s after the end of 'Y' fraction time (from t = .0029 s to t = 0.0039 s, Note – Thickness between the substrate-coating interface and the HAZ-substrate interface is 80 µm, and that from the top of the coating to the substrate-coating interface is 10 µm), Boundary conditions equations 21 and 23, and initial condition $T(z_{TC},0)=1258K$, where z_{TC} is the top of the coating which has been assumed laser sintered from 25 µm thickness powder to 10 µm thickness in the 'X' fraction time and the time of zero indicates the start of the 'Y' fraction time for the revised analysis

CONCLUSIONS

Laser sintering of nanocrystalline diamond powders is an ultra-fast, non-equilibrium process that provides a unique opportunity to produce fairly thick DLC coatings at low substrate temperature. In this paper, a finite-element based model of laser sintering is developed for the determination of temperature distribution in the single powder layer. Temperature distribution in the powder layer due to laser irradiation has been studied for a hypothetical steady state and a close to real transient condition.

1. Raman spectroscopy of the optimum parameter sample showed the presence of DLC and XRD diffraction pattern confirmed it with a peak at 26.61^0. SEM images displayed a near-smooth and continuous coating with occasional globules because of solidification and re-solidification of impurities.
2. The present thermal model is able to predict temperature distribution in the powder layer including the effect of constant heat flux distribution of laser beam, effective thermal conductivity of the powder layer, bed density and temperature-dependent thermal properties of powder material.
3. Finite element analysis of thermal energy transport of this process showed that the majority of time in laser heating is spent on densification and phase transition. It also demonstrates that sintering of nano-diamond powder takes place at substantially lower temperatures (solid state).
4. The model has capabilities for predicting coating depth, interface temperature and size of heat affected zone.

REFERENCES

[1]. P. F. Jacobs, Rapid Prototyping & Manufacturing: Fundamentals of Sterolithography, 1992, Society of Manufacturing Engineers.

[2]. G. Bugeda, M. Cervera, G. Lombera, "Numerical prediction of temperature and density distribution in selective laser sintering process," *Rapid Prototyping Journal*, 5, 1, (1999) 21

[3]. T. Childs, A. Tontowi, "Selective laser sintering of a crystalline and glass-filled crystalline polymer: Experiments and simulations," Proc. Inst. Mech. Engrs, 215 (2001) 1481

[4]. M. Agarwala, D. Bourell, J. Beaman, H. Marcus, J. Barlow, "Direct selective laser sintering of metals," Rapid Prototyping Journal, 1, 1, (1995) 26

[5]. Y. Zhang, A. Faghri, "Melting of a sub-cooled mixed powder bed with constant heat fluxing" International Journal of Heat and Mass Transfer, 42 (1998) 775

[6]. B. Van der Schueren, J. Kruth, "Powder deposition in selective metal powder sintering", Rapid Prototyping Journal, 1, 3, (1995) 23

[7]. Z. Macedo, A. Hernandes, "Laser sintering of $Bi_4Ti_3O_{12}$ ferroelectric ceramics" Materials Letters, 55, 4, (2002) 217

[8]. V. Danilenko, "Phase diagram of nanocarbon" Combustion, Explosion and Shock Waves, 41, 4, (2005) 460

[9]. H. Zhu, R. Averback, “Sintering Processes of two nanoparticles: a study by molecular-dynamics simulations,” Philosophical Magazine Letters, 73, 1, (1996) 27

[10]. P. Arato, L. Bartha, R. Porat, S. Berger, A. Rosen, “Solid or liquid phase sintering of nanocrystalline WC/Co hardmetals.” Nanostructured Materials, 10, 2, (1998) 245

[11]. J. Chen, S. Deng, J. Chen, Z. Yu, N. Xu, “Graphitization of nanodiamond powder annealed in argon ambient,” Applied Physics Letters, 74, 24 (1999) 3651

[12]. T. Friedman, J. Sullivan, J. Knapp, D. Tallant, D. Follstaedt, D. Medlin, P. Mirkarimi, “Thick stress-free amorphous-tetrahedral carbon films with hardness near that of diamond,” Applied Physics Letters, 71, 26, (1997) 3820

[13]. E. Liu, B. Blanpain, X. Shi, J. Celis, H. Tan, B. Tay, L. Cheah, J. Roos, “Tribological behavior of different diamond-like carbon materials,” Surface and Coatings Technology, 106 (1998) 72

[14]. E. Liu, X. Shi, B. Tay, L. Cheah, H. Tan, J. Shi, Z. Sun, “Micro-Raman spectroscopic analysis of tetrahedral amorphous carbon films deposited under varying conditions,” Journal of Applied Physics, 86, 11 (1999) 6078.

[15]. E. Liu, J. Gao, A. Zeng, B. Tay, X. Shi, “Tribological behavior of nanocomposite diamondlike carbon-aluminum films,” Material Research Society Symposium Proceedings, 695 (2002) 231

[16]. H. Dimigen, H. Hubsch, R. Memming, “Tribological and electrical properties of metal-containing hydrogenated carbon films,” Applied Physics Letters, 50, 16 (1987) 1056

[17]. F. Dabby, U. Paek, “High-intense laser-induced vaporization and explosion of solid material” IEEE Journal of Quantum Electronics, 8, 2 (1972) 106

[18]. S. Noguchi, E. Ohmura, L. Miyamoto, “Analysis on resin removal in laser drilling of printed circuit board,” Proceedings of the International Society for Optical Engineering (SPIE), 4830 (2003) 46

[19]. V. Mazhukin, I. Smurov, G. Flamant, “Overheated metastable states in pulsed laser action on ceramics,” Journal of Applied Physics, 78 (1995) 1259

[20]. R. Nair, W. Jiang, P. Molian, “Synthesis of diamond-like carbon coatings on aluminum 6061 T-91 substrates by laser sintering of ultra-nanocrystalline diamond powders,” Journal of Surface & Coatings Technology, 202, 13 (2008) 2935

[21]. N. Vail, B. Balasubramaian, J. Barlow, H. Marcus, “A thermal model of polymer degradation during selective laser sintering of polymer coated ceramic powders,” Rapid Prototyping Journal, 2, 3 (1996) 24

[22]. R. German, “Supersolidus liquid phase sintering. Part II: Densification theory”, International Journal of Powder Metallurgy, 26, 1 (1990) 35

[23]. J. Nelson, S. Xue, J. Barlow, J. Beaman, H. Marcus, D. Bourell, D. L. “Model of the selective laser sintering of bisphenol – A polycarbonate,” Ind. Eng. Chem. Res., 32 (1993) 2305

[24]. J. Nelson, N. Vail, J. Barlow, J. Beaman, D. Bourell, H. Marcus, “Selective laser sintering of polymer-coated silicon carbide powders,” Ind. Eng. Chem. Res., 34 (1995) 1641

[25]. F. Incropera, D. DeWitt, Fundamentals of Heat and Mass Transfer, Fourth Edition, John Wiley & Sons.

[26]. S. Yagi, D. Kunii, “Studies in the effective thermal conductivities in packed beds,” American Institute of Chemical Engineering Journal, 3, 3 (1957), 373

[27]. Y. Touloukian, C. Ho, Editions -Thermophysical Properties of Matter, The TPRC Data Series (13 volumes on thermophysical properties: thermal conductivity, specific heat, thermal radiative, thermal diffusivity, and thermal linear expansion), (1970-1977). Plenum Press, New York.

[28]. J. Wilks, E. Wilks, Properties and Applications of Diamond, 1991, Butterworth-Heinemann Ltd, Linacre House, Jordan Hill, Oxford OX2 8DP.

[29]. H. Pierson, Handbook of Carbon, Graphite, Diamond and Fullerenes, 1993, Noyes Publications, Mill Road, Park Ridge, New Jersey 07656, U.S.A.

[30]. MatWeb.com, Online Materials Database. http://www.matweb.com, Properties of Aluminum 6061 T-91, Retrieved – January 1, 2007.

[31]. J. Ouyang, S. Nowotny, A. Richter, E. Beyer, “Laser cladding of yttria partially stabilized ZrO2 (YPSZ) ceramic coatings on aluminum alloys,” Ceramics International, 27 (2001) 15

[32]. G. Malaczynski, A. Hamdi, A. ElmoursI, X. Qiu, “Diamond-like carbon coating for aluminum 390 alloy – automotive applications,” Surface and Coatings Technology, 93 (1997) 280

[33]. S. Sih, J. Barlow, “The prediction of emissivity and thermal conductivity of powder beds,” Particulate Science and Technology, 22 (2004) 427

[34]. Zaitsev, Optical properties of diamond: A data handbook, 2001, Springer, NY

[35]. M. Seal, “Graphitization of Diamond” Nature,185 (1960) 522

[36]. T. Evans, P. James, “A Study of the Transformation of Diamond to Graphite,” Proceedings *of the Royal Society of London, Series A, Mathematical and Physical Sciences*, 277, 1369 (1964) 260

[37]. J. Wang, G. Yang, “Phase transformation between diamond and graphite in preparation of diamonds by pulsed-laser induced liquid–solid interface reaction,” Journal of Physics: Condensed Matter, 11, 37, (1999) 7089

[38]. Vereshchagin, “Phase Diagram of Ultrafine Carbon,” Combustion, Explosion, and Shock Waves, 38, 3 (2002), 358

[39]. S. H. Lee, S. C. Lee, K. R. Lee, K. H. Lee, J. G. Lee, "Metastable Site in Amorphous Carbon Lattice Generated by Rapid Quenching of Liquid Diamond," Nanotech, Vol. 2,Technical Proceedings of the 2002 International Conference on Computational Nanoscience and Nanotechnology, (2002)466

[40]. P. Reinke, G. Francz, P. Oelhafen, J. Ullmann, "Structural changes in diamond and amorphous carbon induced by low-energy ion irradiation," Physical Review B, 54, 10 (1996) 7068

[41]. L. Nistor, V. Ralchenko, I. Vlasov, A. Khomich, R. Khmelnitskii, P. Potapov, J. Van Landuyt, "Formation of Amorphous Carbon and Graphite in CVD Diamond upon Annealing," Physica status solidi. A, Applied Research, 186, 2 (2001) 207

[42]. J. Qian, C. Pantea, J. Huang, T. Zerda, Y. Zhao, "Graphitization of diamond powders of different sizes at high pressure-high temperature," Carbon, 42 (2004) 2691

[43]. M. Shamsa, W. Liu, A. Balandin, C. Casiraghi, W. Milne, A. Ferrari, "Thermal conductivity of diamond-like carbon films," Applied Physics Letters, 89, 161921 (2006) 1